Sub-nanometer level model validation of the SIM interferometer

Robert P. Korechoff, Daniel Hoppe, Xu Wang

Jet Propulsion Laboratory, California Institute of Technology, Pasadena, CA USA 91109-8099

ABSTRACT

The Space Interferometer Mission (SIM) flight instrument will not undergo a full performance, end-to-end system test on the ground due to a number of constraints. Thus, analysis and physics-based models will play a significant role in providing confidence that SIM will meet its science goals on orbit. The various models themselves are validated against the experimental results of several "picometer" testbeds. In this paper we describe a set of models that are used to predict the magnitude and functional form of a class of field-dependent systematic errors for the science and guide interferometers. This set of models is validated by comparing predictions with the experimental results obtained from the MicroArcsecond Metrology (MAM) testbed and the Diffraction testbed (DTB). The metric for validation is provided by the SIM astrometric error budget.

Keywords: SIM, MAM, interferometer, modeling, astrometry

1. INTRODUCTION

1.1 Overview of SIM sensor systems

The Space Interferometry Mission (SIM) instrument is being designed to make microarcsecond-level measurements of the position of stars [Ref. 1]. SIM consists of four, white light Michelson stellar interferometers on a single structure. Two of the interferometers are identified as science with distinct baselines (only one is active at a time) and two interferometers are identified as guide and share a common baseline. All interferometer baselines are defined by the vertices of hollow corner cubes. The guide interferometers act as fine guidance sensors, and give the pointing of the guide baseline in inertial space at the microarcsecond level. However, the objective is microarcsecond knowledge of the science baseline orientation. This is accomplished by determining the orientation of the science baseline relative to the guide baseline with an optical truss termed the *external* metrology system.[1] Thus, we may divide the SIM instrument into three optical sensor systems: (1) science interferometer, (2) guide interferometers, and (3) external metrology truss. These three sensors are assumed to be separable to first order and therefore may be characterized individually. To that end, several picometer-level[2] testbeds have been developed to demonstrate the technology required for the sensor systems and, in some cases, substantial sub-assemblies of the sensor systems.

The testbeds function in another capacity besides technology demonstrations; they also generate data that can be used to validate picometer-level models that will be sued to predict the flight system performance. The models, in turn, help elucidate the behavior of the testbeds; this increased understanding can be utilized to improve the design of the SIM instrument. In this paper we will primarily be concerned with the MicroArcsecond Metrology (MAM) testbed and its application to the science and guide interferometer sensor systems. To a lesser extent, we will discuss the Diffraction Testbed (DTB).

---

[1] In order to completely define the science baseline in inertial space a "roll" sensor is also required.

[2] Besides the obvious difference in precision, picometer- and nanometer-level have an additional meaning in the SIM instrument lexicon. Whereas nanometer phenomena are sensed *and* controlled, picometer phenomena are only sensed.

1.2 Overview of the MAM testbed

The observable quantity measured by the SIM science interferometer is called the external delay which is illustrated in Fig. 1. Knowledge of the external delay and the magnitude of the science baseline allows one to compute the angle between the line of sight to the observed object (star unit vector) and the science baseline. The external delay cannot be measured directly but can be deduced from two measurements of optical path difference (OPD). The first measurement is the OPD from the observed object to the interferometer beam splitter (see Fig. 1) via the two arms of the interferometer. This measurement is derived from the spectrally dispersed white light (starlight) fringe. The second measurement is the OPD between the beam splitter and the fiducials (*i.e.*, corner cube vertices) defining the science baseline. This measurement comes from the *internal* metrology system. In an ideal system the internal metrology beams would precisely monitor changes in the starlight optical path in each arm of the interferometer. Deviations from this ideal behavior result from systematic biases and random noise. The purpose of the MAM testbed is to demonstrate that these bias and noise terms do not exceed a level specified by the SIM astrometric error budget [Ref. 2].

A schematic layout of the MAM testbed is shown in Fig. 2. The testbed consists of two principal pieces, namely the light source termed the inverse interferometer pseudostar (IIPS) and the test article (TA). The IIPS is a surrogate for a stellar source while the TA simulates the science interferometer sensor. The key to success of the testbed is the use of metrology on the IIPS side, as well as the TA side, to monitor changes in the starlight optical path. In fact, it is a general rule that in order to perform a picometer-level measurement, the entire non-common starlight optical path must be monitored by a metrology beam; this allows one to remove fluctuations in the geometric path length due to dynamics and thermal effects by subtracting the phase changes of the two beams.

The IIPS introduces external delay between its two arms by physically translating two optical assemblies, hereafter called towers, in two degrees of freedom with respect to the IIPS beam splitter. The OPD in each arm, relative to the center of the field, is given by Eq. (1).

$$OPD_{\pm} = \pm x + y + \sqrt{z^2 + x^2 + y^2} - z \approx \pm x + y + \frac{x^2 + y^2}{2z} \quad , \tag{1}$$

where x and y are displacements parallel and perpendicular to the interferometer baseline and z is a fixed distance (800 mm) from the final tower mirror to the baseline corner cubes. The translations x and y vary within a circle of radius 100 mm. From Eq. (1) it is clear that the path length difference between the two IIPS arms (*i.e.*, the external delay) is precisely 2x giving a total one-way range of ±200 mm. Note that the external delay is independent of y; this is useful when we want to remove certain bias terms are described in Sec. 1.3.

1.3 Field dependent bias terms

The SIM instrument operates in two basic modes, so called wide angle (WA) and narrow angle (NA). The WA mode covers a patch of sky (called a tile) 15 degrees in diameter while the NA mode coverage is 1 degree in diameter. Both modes involve macro changes[3] in the pointing of the science interferometer collecting optics (called siderostats) and adjustments to the optical path in one arm depending of the field point being observed. These macro configuration changes, resulting from a change in field angle, produce a class of systematic biases to the measurement of the external delay. Because these biases are explicit functions of field angle, they are termed field dependent (FD) biases. These biases can be classified in three categories: (1) diffraction, (2) beam walk, and (3) corner cube related phenomena. In this section we give a brief overview of the nature of these FD biases. In Sec. 2 we describe the models for each of these biases in detail.

The diffraction bias term results from two facts: (1) the internal metrology and starlight beams have different wavelengths, beam geometries, and propagation lengths, and (2) the pathlength in one arm of the interferometer must be varied to compensate for changes in the external delay as the field point changes. The change in the average phase of the

[3] Macro changes to the system configuration can be thought of as intentional, or commanded, changes. This is to be contrasted with micro system configuration changes that, in general, are smaller in magnitude and result from thermal distortions and dynamic disturbances.

metrology and starlight beams can be thought of as composed of a geometric part and a diffraction part. Since the metrology and starlight beams travel the same path[4] the geometric contribution to phase change is removed by the data processing leaving the difference of the diffraction terms. Although the metrology and starlight beams have different wavelengths, beam geometries, and propagation path lengths, the parameter of interest when comparing differences in the diffraction terms is the Fresnel number. The Fresnel number is a function of wavelength, beam geometry and propagation pathlength as indicated in Eq. (2) below.

$$N_F = \frac{w^2}{\lambda z} \quad , \tag{2}$$

where w is half the characteristic dimension of the diffracting aperture (*i.e.*, radius for a circle or half the side for a square), λ is the wavelength, and z is the propagation distance. Beams that differ in wavelength, geometry, and propagation length, but have the same Fresnel number, will have the same diffraction term. Based

The beam walk bias term refers to the path length change that results from the translation of a beam over the imperfect surface of an optical component such as a mirror. That is, there is a change in the average phase of the beam without any change in the position of the optic. The beam walk bias term is a function of the beam geometry, the rms surface figure error, the power spectral density (PSD) function of the surface profile, and the beam translation distance. In order to model beam walk in a deterministic manner one would need to know the surface profile of each optic with high spatial resolution and the terminal points of the beam translation relative to the surface profile. Rather than a deterministic calculation, our beam walk model relies on a statistical approach. Beam walk can result from both field independent (FI) and dependent processes. For example, misalignment of a mirror due to thermal gradients will produce FI beam walk on the downstream optics. On the other hand, axial translation of the delay line optic (a corner cube) on rails that are misaligned with respect to the beam propagation direction will produce a FD beam walk.

The baselines of the four SIM interferometers are defined by corner cubes as previously mentioned. The corner cubes are also the only components in the instrument that the internal and external metrology beams have in common. For the science baselines, the corner cubes are embedded in the siderostat mirrors and thus articulate as the interferometer observes different stars in a particular tile. As the corner cubes articulate the internal and external metrology beams are incident on the cube facets at changing angles. As a result of varying angles of incidence there are changes in the average phase of the metrology beams due to changes in reflection phase shifts and dihedral errors. The design of the corner cube surfaces calls for coating with unprotected gold. Thus, the reflection phase shift is a function of the polarization state of the incident field and varies continuously with angle of incidence. Dihedral errors refer to the fact that the corner cube facet normals are not exactly mutually perpendicular. This gives rise to geometric path length errors that depend on reflection sequence and point of incidence.

There are three additional FD corner cube errors to consider: (1) corner cube vertex/siderostat offset, (2) non-common vertices, and (3) beam walk. The first effect refers to the fact that the corner cube vertex is offset from the surface of the siderostat mirror. This introduces a non-common optical path between the starlight and the internal metrology that varies with field angle. The second item results from the need to accommodate both internal and external metrology beams whose propagation directions exceed the field of view of a single corner cube. We have effectively extended the field of view of the corner cubes by utilizing assemblies that are multiple corner cubes. In theory these multiple corner cubes have a common vertex but in practice they do not due to fabrication limitations. The non-common vertex bias does not appear in MAM because there is no external metrology system; however, this error is important for the flight system so we mention it here for completeness. Finally, there are two types of beam walk to consider. The corner cube articulation axes will not pass through the vertex. The resulting translation of the corner cube facets relative to the fixed metrology beams will produce beam walk of the type described above. Another type of beam walk also occurs because the metrology beam footprints on the facets change shape as the corner cubes articulate.

In this section we have provided an introduction to the nature of the FD biases encountered in the MAM testbed. In the next section we give the details concerning the modeling of these bias terms.

---

[4] The metrology propagates through the system in double pass but the change in its phase is multiplied by 0.5. This removes the geometric contribution when the difference between the metrology and starlight phase changes are subtracted.

2. FIELD DEPENDENT MODELS

2.1 Diffraction

The computer code used to model diffraction terms for the SIM flight system and testbeds was developed at the Lockheed Martin Advanced Technology Center by R. Benson [Ref. 3]. In this section we briefly describe some of the physical principles and numerical techniques on which the code is based. The SIM diffraction code is a numerical implementation of the scalar, paraxial theory as described in Ref. 4. Diffraction calculations for SIM consist of a series of free-space propagations between various planes within the optical system. The Fresnel numbers for these propagations vary over a wide range of values implying that both near field and far field calculations are required.[5]

The diffraction calculation can be formulated in a number of ways. Consider an aperture Σ in the x-y plane. Let a field of wavelength λ be incident on the aperture. We wish to calculate the field for an arbitrary observation point $p_0 = (x,y,z)$. Following Ref. 4, we may write the complex field at p_0 in two formulations[6]

$$E(p_0) = \frac{1}{i\lambda}\iint_{\Sigma} E(p_1)\frac{\exp(ikr_{01})}{z}d\Sigma \quad , \tag{3a}$$

$$E(p_0) = \iint A(f_x,f_y,0)\exp\left(ikz\sqrt{1-(\lambda f_x)^2-(\lambda f_y)^2}\right)\exp\left[i2\pi(xf_x+yf_y)\right]df_x df_y \quad , \tag{3b}$$

where k is the wave number $2\pi/\lambda$, p_1 is in Σ, r_{01} is the distance from p_1 to p_0, $f_q = \alpha/\lambda$ is the spatial frequency associated with the direction cosine α along the q axis, A is the Fourier transform of the field in the aperture Σ. The expressions given in Eq. (3a) and (3b) may be called the point source, or direct method, and the angular spectrum method respectively. Although the two expressions are mathematically equivalent, there are computational advantages to having the capability of evaluating either expression depending on circumstances. The expressions in Eq. (3) are simplified by evoking the assumption that the propagation distance is much greater than the maximum linear dimension of either the aperture S or the region of interest in the observation plane. Expanding the appropriate square roots yields

$$r_{01} \approx z + \frac{(x_1-x_0)^2}{2z} + \frac{(y_1-y_0)^2}{2z} \quad , \tag{4a}$$

$$\sqrt{1-(\lambda f_x)^2-(\lambda f_y)^2} \approx 1-\frac{1}{2}\left[(\lambda f_x)^2+(\lambda f_y)^2\right] \quad , \tag{4b}$$

Substituting Eqs. (4) into (3) gives the following

$$E(p_0) = \frac{e^{ikz}}{i\lambda z}\exp\left[\frac{ik}{2z}(x_0^2+y_0^2)\right]\iint E(p_1)\exp\left[\frac{ik}{2z}(x_1^2+y_1^2)\right]\exp\left[\frac{i2\pi}{2z}(x_0x_1+y_0y_1)\right]dx_1dy \quad , \tag{5a}$$

$$E(p_0) = e^{ikz}\iint A(f_x,f_y,0)\exp\left[-i\pi\lambda z(f_x^2+f_y^2)\right]\exp\left[i2\pi(xf_x+yf_y)\right]df_x df_y \quad . \tag{5b}$$

Inspection of Eq. (5) shows that for a fixed grid (*e.g.*, $N\Delta x$) size there is an exponential function within the integral of the direct method with an argument that is proportional to the Fresnel number; for the angular spectrum method the argument is inversely proportional to the Fresnel number. Therefore, the integrand for the direct method becomes more oscillatory with increasing Fresnel number while the integrand for the angular spectrum method becomes more

---

[5] Near and far field diffraction calculations are often referred to as Fresnel and Fraunhofer approximations of the diffraction problem respectively. Technically, the Fresnel approximation covers both the near and far field; that is, the Fraunhofer integral is a special case of the Fresnel integral.

[6] In Eq. (2) the obliquity factor has been approximated as unity in keeping with the paraxial assumption.

oscillatory with decreasing Fresnel number. Following the aliasing argument presented by Dutta and Benson [Ref. 3], we can cast the choice between Eqs. (5a) and (5b) in terms of propagation length as follows

$$z \le \frac{(N\Delta x)^2}{\lambda N} \Rightarrow \text{angular spectrum method} \quad , \tag{6a}$$

$$z \ge \frac{(N\Delta x)^2}{\lambda N} \Rightarrow \text{direct method} \quad . \tag{6b}$$

This trade in computational accuracy, as a function of Fresnel number, between the direct and angular spectrum methods was tested for a series of cases with closed-form solutions and demonstrated the need for both algorithms if a wide range of Fresnel numbers are required [Ref. 2]. Thus, the diffraction code chooses the appropriate formulation based on the criteria given in Eq. (6).

Both the direct and angular spectrum methods require numerical implementation of a two-dimensional Fourier transform that is usually called a discrete Fourier transform (DFT). A subset of DFT algorithms, called fast Fourier transforms (FFT), have been developed for high computational efficiency. However, FFTs come with certain restrictions on sample spacing in the two planes of interest. That is, selecting the sampling interval in one plane determines the sampling interval in the other plane. The general DFT does not contain this sampling restriction. Thus, what one sacrifices in computational speed is offset by the ability to tailor the sample spacing to the aperture of interest. However, one can improve the computational efficiency of the DFT by using the chirp z-transform (CZT) [Refs. 6, 7]. The CZT algorithm allows one to formulate the DFT as a convolution that can then be evaluated by FFT thus improving the computational speed over the DFT while retaining the freedom to choose the grid spacing in the transform plane. For the angular spectrum method, the diffraction code evaluates the Fourier transforms by a FFT. For the direct method, the code will use a FFT or the CZT depending on the user's choice for the grid spacing in the final plane.

Perhaps the most crucial issue with regard to diffraction is the accuracy of the code. This is a two-part question, namely (1) what is the accuracy requirement for SIM, and (2) how does one test the code. The answer to the first part of the question comes from the SIM astrometric error budget that requires knowledge of certain types of diffraction effects at the few picometer level.[7] The second part of the question required a two-step answer. Step 1 consisted of a computational check using a case amenable to implementation by an independent calculation using Mathematica software. This step checked that the paraxial, scalar diffraction equations were correctly coded in the Fortran program and gave an indication of the accuracy as a function of sample spacing. To make the calculation tractable in Mathematica we chose a case with circular symmetry and calculated the average phase of the beam in the observation plane. The circular symmetry allowed us to replace two-dimensional DFTs with one-dimensional Fourier-Bessel transforms (also known as Hankel transform of zero order). The Mathematica calculation was carried out with a working precision of 34 digits[8] and was taken as the "correct" answer. The difference in average phase, converted to path length (λ = 1.319 μm), between the Fortran diffraction code and the Mathematica calculation, as a function of sample spacing, is given in Table 1. Based on the convergence of the two methods at the picometer level, as a function of sample spacing, we concluded that the Fortran diffraction code algorithms were properly coded and had the necessary precision.

Table 1: Comparison of Fortran and Mathematica diffraction calculations

Grid size (mm)	Grid pts.	Sample spacing (μm)	Average phase difference (pm)
50	2048	24.4	16
25	2048	12.2	4
25	4096	6.1	1

[7] The metrology beam launchers have a requirement on an error called cyclic error that is 3 pm.

[8] A working precision of 34 is the precision used for internal calculations. We used the default setting for the precision of the final answer (precision goal parameter) which means the calculation strives for 10 digits less or 24 digits of precision.

The Fortran code and the Mathematica calculations embody the same paraxial, scalar approximations. Thus, step 2 of the verification process was to check the code against a set of measurements. A special testbed, dubbed the Diffraction Testbed (DTB), was designed and constructed at the Lockheed Martin Advanced Technology Center for this purpose [Ref. 8]. The details of the configuration, operation, and data processing of the DTB are outside the scope of this paper but suffice it to say that the testbed was designed to operate with SIM-like starlight and metrology Fresnel numbers. There were several requirements levied on the agreement between the diffraction model and the DTB results but the most germane for our discussion is the following: The rms difference between the DTB and model OPD residuals (obtained by removing linear and quadractic terms) shall be less than 75 pm over a 30-cm mechanical delay line stroke. The model and testbed rms difference was 43 pm and thus met this requirement with margin. This was a truly impressive achievement for both the testbed and the model. It should also be noted that the DTB is the first successful SIM pico-level testbed.

2.2 Beam walk

The beam walk model is a statistical calculation. The quantity calculated is the standard deviation of a zero-mean distribution of path length changes that result from translation of a beam of given geometry by a distance $\vec{s}$ over an ensemble of surfaces that are all characterized by a specified diameter, rms surface figure error, and PSD function for the surface error. The general expression for the variance of this path length change, σ^2, is given by the following expression.

$$\sigma^2 = \left\langle \left| \frac{1}{A}\int x(\vec{r})\,d\vec{r} - \frac{1}{A}\int x(\vec{r}+\vec{s})\,d\vec{r} \right|^2 \right\rangle \quad , \tag{7}$$

where x is the deviation of the surface height from the mean at position $\vec{r}$, A is the area of the beam, and <...> represents an average over an ensemble of surfaces. The beam walk calculation is based on a formalism used for random processes in atmospheric turbulence problems. The key concept is the representation of the optic surface in Eq. (7) by a stochastic Fourier Stieltjes integral as described in Appendix A of Ref. 9 and given in Eq. (8). The use of this integral representation for beam walk analysis was originally developed at JPL by M. Colavita.

$$x(\vec{r}) = \int_{-\infty}^{\infty} \exp\left(-i2\pi\vec{f}\cdot\vec{r}\right) d\omega\left(\vec{f}\right) \quad , \tag{8}$$

where f is the spatial frequency normalized to the mirror diameter and dw(f) is called the random amplitude. The random amplitude has the following property

$$\left\langle d\omega\left(\vec{f}\right) d\omega\left(\vec{f}'\right)\right\rangle = PSD\left(\vec{f}\right)\delta\left(\vec{f}-\vec{f}'\right)d\vec{f}\,d\vec{f}' \quad . \tag{9}$$

In order the carry out this calculation we make several assumptions that are listed here:

- The PSD function is radially symmetric; hence, the path length change only depends on the magnitude of the walk and not the direction.
- The PSD function is directly proportional to f^p. If PSD data are available we fit for the exponent p. If no data are available we usually assume p = -2.5. The minimum spatial frequency considered is 1 cycle/mirror diameters.
- One half of the surface error power is contained in spatial frequencies greater than 1 cycle/mirror diameter.

Using Eqs. (7) – (9) and the assumptions listed above, the general form for the path length change variance can be written as an integral of spatial frequencies over the PSD function, normalized to half the wavefront variance, multiplied by a transfer or filter function H.

$$\sigma^2 = 2\pi\int_1^{\infty} PSD(f)H(f)f\,df \quad . \tag{10}$$

As an example, the filter function for a uniform circular beam of diameter d, normalized to the mirror diameter, is

$$H(f) = 2\left[1 - J_0(2\pi f s)\right]\left[\frac{2J_1(\pi f d)}{\pi f d}\right]^2 \quad , \tag{11}$$

where J_0 and J_1 are Bessel functions of the first kind of order 0 and 1 respectively.

We are often interested in a quantity called the beam walk sensitivity that is the first derivative of the path length change standard deviation with respect to beam translation. For a circular beam and typical beam/mirror dimensions, it can be easily shown that s is a linear function of s. Expanding J_0 as a power series of its argument yields [Ref. 10]

$$J_0(z) \cong 1 - \frac{z^2}{4} \qquad \text{for } z << 1 \quad . \tag{12}$$

Substituting Eqs. (11) and (12) into (10) shows that s is directly proportional to s. Thus, for this case and many others, the beam walk sensitivity is independent of the magnitude of the beam translation.

A secondary goal of the DTB was to validate the beam walk model described above. Note that it is difficult to assign a pass/fail criterion to this test due to the statistical nature of the model. The beam walk sensitivity results for the testbed and the model were 0.53 and 0.90 pm/μm respectively. Analysis of various model uncertainties showed that the model prediction could reasonably be 0.74 pm/μm. It was concluded that the agreement between the testbed and the model was close enough that there is unlikely to be anything substantially incorrect about the model assumptions or computational techniques. A detail discussion of the beam walk test and model results can be found in Ref. 8.

2.3 Corner cubes

2.3.1 Dihedral errors

The dihedral error between two corner cube facets is the difference of the angle between the surface normals and 90 degrees. These errors result in two types of geometric path length changes as the corner cube articulates, namely OPD_1 within the corner cube and OPD_2 due to the fact that a given ray exiting the corner cube is no longer propagating anti-parallel to the incident ray direction. An expression for the first type of OPD between two facets is easily derived. Consider the path length of a ray propagating between facet i and j. The facets are defined by their unit normals, n_i and n_j, and the corner cube vertex q. Let the ray of interest be incident on facet i at the point p_i and propagate between surfaces i and j along the unit vector v. Then the propagation distance t between facets i and j is given by the following equation.

$$t = \frac{\langle q - p_i, n_j \rangle}{\langle v, n_j \rangle} \quad , \tag{13}$$

where <a,b> is the inner product between vectors a and b. Let ψ be the dihedral error between facets i and j. To first order in ψ we may write $n_j = r + \psi n_i$ where r is the unit normal to facet j with no dihedral error present. Substituting this expression for n_j into Eq. (13) yields after some manipulation the following

$$OPD_1 = t - \frac{\langle q - p_i, r \rangle}{\langle v, r \rangle} = -\psi \langle q - p_i, r \rangle \frac{\langle v, n_i \rangle}{\langle v, r \rangle^2} \quad . \tag{14}$$

We note that OPD_1 is directly proportional to the dihedral error and the distance between the ray intercept on facet i and the corner cube vertex. In addition, the proportionality constant is a function of the angle of incidence at facet i.

To calculate OPD_2 we need to know the propagation direction of a ray exiting the corner cube compared to the incident ray direction, that is, the angle of deviation θ. It can be shown [Ref. 11] that

$$\theta = 2|v \times \psi| \quad , \tag{15}$$

where v is a unit vector in the incident propagation direction and ψ is a vector containing the three dihedral errors defined as follows when the subscripts denote the reflection sequence.

$$\langle n_1, n_2 \rangle = \psi_3 \; ; \quad \langle n_1, n_3 \rangle = -\psi_2 \; ; \quad \langle n_2, n_3 \rangle = \psi_1 \quad . \tag{16}$$

Using the expression in Eq. (15) for the propagation deviation angle, the value of OPD_2 after propagating a distance L is given by

$$OPD_2 = 2L|v \times \psi|^2 \quad . \tag{17}$$

Comparing Eqs. (14) and (17), it is clear that the OPD within the corner cube depends on the dihedral error to first order while the OPD resulting from misalignment is a second order effect. The implication of the above analysis is that each ray will have its particular OPD based on its reflection sequence and point of incidence.

2.3.2 Reflection phase shifts

Reflection phase shifts are a function of angle of incidence, wavelength, index of refraction of the reflecting surface, and polarization state. In the case of MAM only the articulation of the corner cubes at the siderostats will produce significant changes in the reflection phase shifts. The corner cubes are coated with unprotected gold and hence have a complex index of refraction. The reflection phase shifts are given by the well-known Fresnel equations. The only issue involves consistency between the Fresnel equations, the directions of the s and p polarization unit vectors before and after the reflection, the sign of the imaginary part of the complex index, and the sign of the spatial phase term for a wave propagating in free space. We have found several inconsistencies between these items in various texts and commercial optical design codes. A complete discussion of these issues can be found in Ref. 12. We can summarize our modeling conventions as follows: (1) The spatial part of the phase of a wave propagating in free space becomes more positive in the direction of propagation. (2) The complex index of refraction is given by $\tilde{n} = n + ik$ where n and k are positive. (3) The positive (zero phase) directions of the incident and reflected p-polarization unit vector point are defined by the cross product s x k where s is the unit vector in the positive s-polarization direction and k is the propagation vector. (4) Finally, the equations for the s- and p-polarization complex amplitude reflection coefficients are given by

$$R_s = -\frac{\sin(\theta_i - \theta_r)}{\sin(\theta_i + \theta_r)} \quad \textit{and} \quad R_p = \frac{\tan(\theta_i - \theta_r)}{\sin(\theta_i + \theta_r)} \quad , \tag{18}$$

where θ_i and θ_r and the angles of incidence and refraction respectively.

2.3.3 Vertex offset

The siderostat mirror articulates over the field of regard to reflect IIPS starlight, defined by the unit vector s, into the TA optical system in a direction specified by the unit vector e. If the corner cube vertex is separated from the siderostat front surface by a distance d along the mirror normal, the unmonitored geometric distance, b, is given by

$$b = d\sqrt{2 + 2\langle s, e \rangle} \quad , \tag{19}$$

where <a,b> is the inner product between the vectors a and b. The unmonitored distance at the center of the field of regard represents a constant offset between starlight and metrology path lengths that can be lumped in with other constant offsets. However, b is a function of field angle; thus, we are really interested in the deviation of b from its value

at the center of the field as a function of field angle. Although we can simply evaluate Eq. (19) for various field points, it is of interest to decompose this deviation into terms of increasing order of the field coordinates.

In the MAM testbed, field angle is specified by the Cartesian coordinates x and y which are displacements from the center of the field along and perpendicular to the TA baseline respectively. Let θ be the angle between the center of the field (x = y = 0) and the vector e. Then we can rewrite Eq. (19) as

$$b(x,y) = \sqrt{2}\, d\sqrt{1+\cos\theta}\,\frac{\sqrt{1+\langle s,e\rangle}}{\sqrt{1+\cos\theta}} = C\sqrt{1+K} \quad , \tag{20}$$

where C is the value of b and the center of the field and

$$K = \frac{y}{R}\frac{\sin\theta}{1+\cos\theta}\left(1-\frac{r^2}{2R^2}\right)-\frac{r^2}{2R^2}\frac{\cos\theta}{1+\cos\theta} \quad , \tag{21}$$

where $r^2 = x^2 + y^2$ and R is the distance between the corner cube vertex and the x-y plane. Expanding the radical in Eq. (20) as a power series in K, we may write the deviation of b from its value at the center of the field as a sum of terms of increasing order of the field coordinates.

$$\textit{linear term} = \frac{C}{2}\frac{y}{R}\frac{\sin\theta}{1+\cos\theta} \quad , \tag{22a}$$

$$\textit{quadratic term} = -\frac{C}{4R^2}\left\{r^2\frac{\cos\theta}{1+\cos\theta}+\frac{y^2}{2}\left(\frac{\sin\theta}{1+\cos\theta}\right)^2\right\} \quad , \tag{22b}$$

$$\textit{cubic term} = \frac{C}{4R^3}\left\{\frac{y^3}{4}\left(\frac{\sin\theta}{1+\cos\theta}\right)^3+\frac{yr^2}{2}\frac{\sin\theta\cos\theta}{(1+\cos\theta)^2}-yr^2\frac{\sin\theta}{1+\cos\theta}\right\} \quad . \tag{22c}$$

3. COMPARISON OF MODELS AND MAM DATA

In Section 2 we described the physical and mathematical bases of the various FD bias models. In some cases the model description applied to a single reflection or propagation path. These equations have been combined with a layout of the MAM testbed to produce system-level predictions. For computational reasons two system models have been developed, namely one for diffraction and one for corner cube phenomena. Beam walk calculations are not included in the results given below.

When comparing the model predictions with MAM data it is convenient to expand the FD bias function, α, in terms of the low-order Zernike polynomials written in Cartesian coordinates as in Eq. (23).

$$\alpha(x,y) = c_0 + c_1 x + c_2 y + c_3\left(x^2+y^2\right)+c_4\left(x^2-y^2\right)+c_5 xy+\ldots, \tag{23}$$

where x and y are the MAM field coordinates parallel and perpendicular to the baseline respectively. Generally, we evaluate c_1, c_2, and c_3. Under certain circumstances we evaluate $c_3 + c_4$ and $c_3 - c_4$ which are the coefficients of x^2 and y^2 respectively. It is important to note that post-processing of the SIM flight system data will remove terms c_0 through c_3. For model validation purposes we compare coefficients c_1, c_2, $c_3 + c_4$, and $c_3 - c_4$.

Validation of the diffraction model was successfully carried out on the DTB. However, in the interest of understanding the behavior of the MAM testbed we compare the model and testbed data for the diffraction bias term. Model validation for the corner cube model is dependent on the comparison between model predictions and testbed data. There are two criteria of interest over the WA field of regard, one pertaining to unprocessed data and one to the residual after SIM-like

post-processing. For the former, the average absolute value of the fractional difference between the model and the testbed data should be less than 20 percent. For the latter case, the rms difference should be less than TBD pm.

In order to facilitate the comparison of the MAM models and experimental results the testbed has been operated in particular modes that isolate, to varying degrees, the various bias terms.[9] To isolate the diffraction term the testbed was run in the TA and IIPS retro modes that utilize only half of the testbed at a time. For example, in the TA retro mode the siderostats are oriented to retro-reflect a monochromatic starlight source that propagates with the internal metrology beam from the TA beam splitter. In this case the TA operates entirely without the IIPS. Because the starlight source has a long coherence length the TA can still produce fringes for large path length differences. Thus, the only macro configuration change in this mode is the path length in the TA arm with the delay line. For the corresponding mode on the IIPS side the siderostats are replaced with large corner cubes that return the metrology and starlight beams. The corner cubes articulate to give them a constant orientation with respect to the starlight and metrology beams and thus remove their FD effects. To isolate the corner cube effects we only examine the terms of the FD bias function for the IIPS plus TA configuration that depend on the coordinate perpendicular to the TA baseline. Motion in this direction maintains a constant path length difference thus producing a constant diffraction contribution. Another potential test of the corner cube model is the IIPS retro test where only the corner cubes articulate. In this case the path lengths in each arm are fixed so that the diffraction term is a constant. At this time the dihedral errors for the corner cubes used in the IIPS retro test have not been measured with sufficient precision. Thus, comparison between the model and IIPS test data will not be available until the tests have been completed, the large corner cubes removed and their dihedral errors re-measured.

3.1 Diffraction results

Table 2 compares the model results with the testbed data for the two tests that were intended to isolate the diffraction terms for the TA and IIPS. The TA retro mode test generates a true one-dimensional bias function in the field variable x because there is no other degree of freedom. Thus, only the coefficients c_1 and $c_3 + c_4$ are meaningful. On the other hand, the IIPS retro test produces a two-dimensional bias function although it is weakly dependent on the y coordinate. Both the model and testbed data show that the diffraction in the IIPS dominates the diffraction in the TA.

Table 2: Comparison of MAM data and model predictions for diffraction terms

	TA retro test		IIPS retro test	
Coefficient	Model	MAM data	Model	MAM data
c_1 (pm/deg)	388	-659	-1974	-2184
c_2 (pm/deg)	N/A	N/A	0.8	60
$c_3 + c_4$ (pm/deg^2)	12	81	-2.6	59
$c_3 - c_4$ (pm/deg^2)	N/A	N/A	-2.6	1.4

3.2 Corner cube results

The three corner cube phenomena described in some detail above have been integrated into a single model called the integrated model. However, it is possible to evaluate each term separately. As an example, one can determine the reflection phase shifts assuming no dihedral errors or vertex offset. Thus, the sum of the individual terms can be compared with the fully integrated model. This exercise has been carried out with results that differ at the few picometer level. We therefore conclude that the coupling between reflection phase shifts, dihedral errors, and vertex offset is negligible for the size errors of interest to MAM and SIM. In addition to demonstrating that coupling between different corner cube bias terms is small, the individual models give insight into which type of corner cube errors dominate the overall bias function. For example we have found that the reflection phase shifts from the two arms largely cancel each other producing a small net bias term. Table 3 presents the c_2 and $c_3 - c_4$ coefficients derived from fits to the MAM measurements for the IIPS plus TA configuration along with the model predictions.

---

[9] Note that all macro changes to the system configuration introduce beam walk which is not included in either the diffraction or corner cube models.

Table 3: Comparison of MAM data and model predictions for corner cube terms

	IIPS +TA	
Coefficient	Model	MAM data
c_1 (pm/deg)	N/A	N/A
c_2 (pm/deg)	1045	1218
$c_3 + c_4$ (pm/deg^2)	N/A	N/A
$c_3 - c_4$ (pm/deg^2)	-41	-26

4. CONCLUSIONS

We have compared modeling results and testbed data for three cases. For the two cases with large linear terms, the agreement between the linear terms is about 10 and 15 percent. For the case with a relative small linear term, the sign and magnitude do not agree. In addition, the testbed tends to measure larger quadratic coefficients than the model predicts. Our conclusion is that the diffraction and corner cube models predict the correct overall behavior of the bias function when these terms dominate other error sources. For example, for the TA retro test the sign and magnitude of the measured linear term is known to fluctuate with metrology and starlight beam alignment. Model validation will proceed as the behavior of the MAM testbed becomes understood better and the measurements more stable.

ACKNOWLEDGEMENTS

The author would like to acknowledge the significant contributions of R. Goullioud (JPL), who has overall responsibility for the MAM testbed and provided valuable oversight of the modeling effort, and J. Shen (JPL), who performed all the MAM data analysis. This research was performed at the Jet Propulsion Laboratory, California Institute of Technology, under contract with the National Aeronautics and Space Administration.

REFERENCES

1. P. Kahn and K. Aaron, "Space Interferometry Mission: Flight system and configuration overview," Proc. of SPIE Vol. 4852, 2002, pp. 33-44.
2. B. Hines et al., "Micro-arcsecond metrology (MAM) testbed overview," Proc. of SPIE Vol. 4852, 2002, pp. 45-56.
3. K. Dutta and R. Benson, "Performance modeling of optical metrology systems," Proc. of SPIE Vol. 4852, 2002, pp. 839-848.
4. J. W. Goodman, *Introduction to Fourier Optics*, McGraw-Hill Book Company, San Francisco, 1968.
5. M. V. Papalexandris and D. C. Redding, "Calculation of diffraction effects on the average phase of an optical field," J. Opt. Soc. Am. A, 17, 2000, pp. 1763-1772.
6. L. R. Rabiner, R. W. Schafer, and C. M. Rader, "The Chirp z-Transform," IEEE Trans. Audio and Electroacoustics, AU-17, 1969, pp. 86-92.
7. S. Roose, B. Brichau, and E. W. Stijns, "An efficient interpolation algorithm for Fourier and diffractive optics," Optics Communications, 97, 1993, pp. 312-318.
8. D. S. Schaechter, Diffraction Testbed Final Report, JPL internal document D-21722, January 14, 2004.
9. A. Ishimaru, Wave Propagation and Scattering in Random Media, IEEE Press, Piscataway, New Jersey, 1997.
10. M. Abramowitz and I. Stegun, *Handbook of Mathematical Functions*, Dover Publications, Inc. New York, 1965.
11. M. Milman, "Corner cube stuff," undated JPL internal memo.
12. G. Kuan and R. Demers, "On Kite, Zemax, and Electric Field Propagation and Reflection," SIM library file 18704, March 17, 2004.

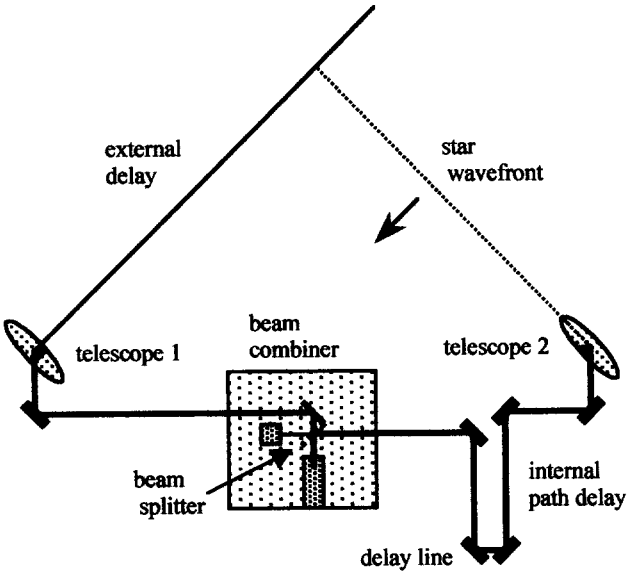

Fig. 1 Schematic of a SIM-like interferometer. The external delay is a function of the angle between the stellar wavefront and the interferometer baseline.

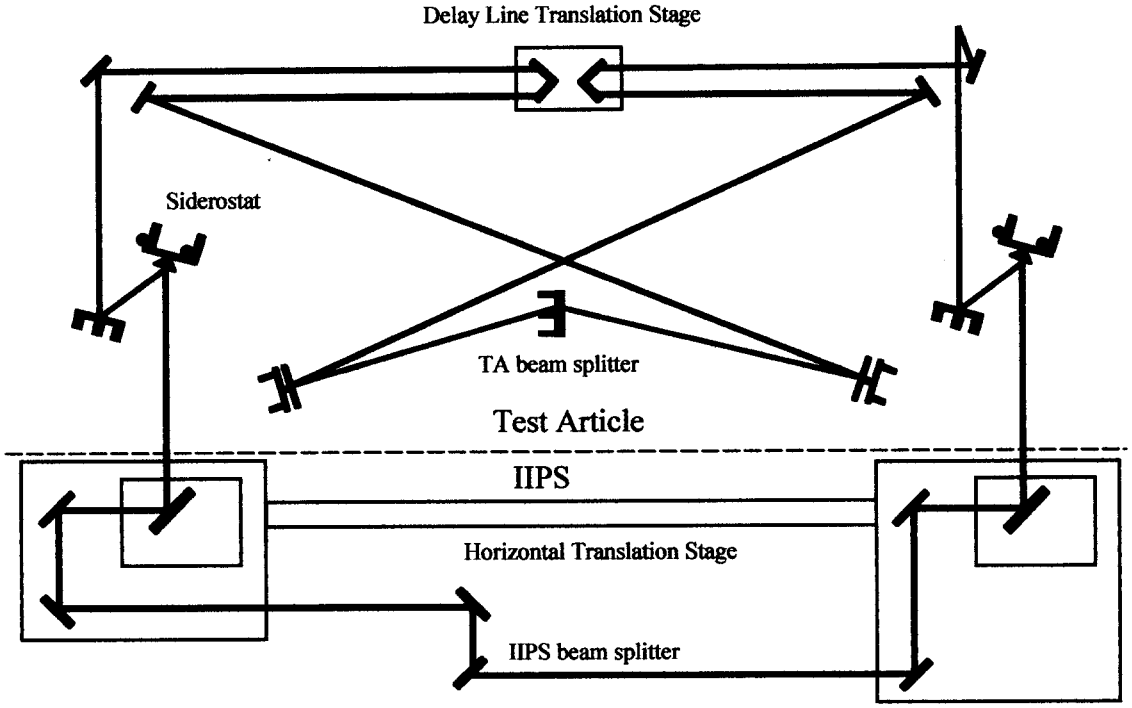

Fig. 2. Schematic of the MAM testbed. The dotted line indicates the boundary between the IIPS and the TA. The non-common paths extend from the IIPS beam splitter to the TA beam splitter.

04-1568

Sub-nanometer level model validation of the SIM interferometer

Robert P. Korechoff*, Daniel J. Hoppe, Xu Wang

Jet Propulsion Laboratory, California Institute of Technology, Pasadena, CA USA 91109-8099

ABSTRACT

The Space Interferometer Mission (SIM) flight instrument will not undergo a full performance, end-to-end system test on the ground due to a number of constraints. Thus, analysis and physics-based models will play a significant role in providing confidence that SIM will meet its science goals on orbit. The various models themselves are validated against the experimental results of several "picometer" testbeds. In this paper we describe a set of models that are used to predict the magnitude and functional form of a class of field-dependent systematic errors for the science and guide interferometers. This set of models is validated by comparing predictions with the experimental results obtained from the MicroArcsecond Metrology (MAM) testbed and the Diffraction testbed (DTB). The metric for validation is provided by the SIM astrometric error budget.

Keywords: SIM, MAM, interferometer, modeling, astrometry

1. INTRODUCTION

1.1 Overview of SIM sensor systems

The Space Interferometry Mission (SIM) instrument is being designed to make microarcsecond-level measurements of the position of stars [Ref. 1]. SIM consists of four, white light Michelson stellar interferometers on a single structure. Two of the interferometers are identified as science with distinct baselines (only one is active at a time) and two interferometers are identified as guide and share a common baseline. All interferometer baselines are defined by the vertices of hollow corner cubes. The guide interferometers act as fine guidance sensors, and give the pointing of the guide baseline in inertial space at the microarcsecond level. However, the objective is microarcsecond knowledge of the science baseline orientation. This is accomplished by determining the orientation of the science baseline relative to the guide baseline with an optical truss termed the *external* metrology system.[1] Thus, we may divide the SIM instrument into three optical sensor systems: (1) science interferometer, (2) guide interferometers, and (3) external metrology truss. These three sensors are assumed to be separable to first order and therefore may be characterized individually. To that end, several picometer-level[2] testbeds have been developed to demonstrate the technology required for the sensor systems and, in some cases, substantial sub-assemblies of the sensor systems.

The testbeds function in another capacity besides technology demonstrations; they also generate data that can be used to validate picometer-level models that will be used to predict the flight system performance. The models, in turn, help elucidate the behavior of the testbeds; this increased understanding can be utilized to improve the design of the SIM instrument. In this paper we will primarily be concerned with the MicroArcsecond Metrology (MAM) testbed and its application to the science and guide interferometer sensor systems. To a lesser extent, we will discuss the Diffraction testbed (DTB).

---

[1] In order to completely define the science baseline in inertial space a "roll" sensor is also required.

[2] Besides the obvious difference in precision, picometer- and nanometer-level have an additional meaning in the SIM instrument lexicon. Whereas nanometer phenomena are sensed *and* controlled, picometer phenomena are only sensed.

*robert.korechoff@jpl.nasa.gov; phone 1 818 354-0083; fax 1 818 393-1916; http://www.jpl.nasa.gov

1.2 Overview of the MAM testbed

The observable quantity measured by the SIM science interferometer is called the external delay which is illustrated in Fig. 1. Knowledge of the external delay and the magnitude of the science baseline allows one to compute the angle between the line of sight to the observed object (star unit vector) and the science baseline. The external delay cannot be measured directly but can be deduced from two measurements of optical path difference (OPD). The first measurement is the OPD from the observed object to the interferometer beam splitter (see Fig. 1) via the two arms of the interferometer. This measurement is derived from the spectrally dispersed white light (starlight) fringe. The second measurement is the OPD between the beam splitter and the fiducials (*i.e.*, corner cube vertices) defining the science baseline. This measurement comes from the *internal* metrology system. In an ideal system the internal metrology beams would precisely monitor changes in the starlight optical path in each arm of the interferometer. Deviations from this ideal behavior result from systematic biases and random noise. The purpose of the MAM testbed is to demonstrate that these bias and noise terms do not exceed a level specified by the SIM astrometric error budget [Ref. 2].

A schematic layout of the MAM testbed is shown in Fig. 2. The testbed consists of two principal pieces, namely the light source termed the inverse interferometer pseudostar (IIPS) and the test article (TA). The IIPS is a surrogate for a stellar source while the TA simulates the science interferometer sensor. The key to success of the testbed is the use of metrology on the IIPS side, as well as the TA side, to monitor changes in the starlight optical path. In fact, it is a general rule that in order to perform a picometer-level measurement, the entire non-common starlight optical path must be monitored by a metrology beam; this allows one to remove fluctuations in the geometric path length due to dynamics and thermal effects by subtracting the phase changes of the two beams.

The IIPS introduces external delay between its two arms by physically translating two optical assemblies, hereafter called towers, in two degrees of freedom with respect to the IIPS beam splitter. The OPD in each arm, relative to the center of the field, is given by Eq. (1).

$$OPD_{\pm} = \pm x - y + \sqrt{R^2 + x^2 + y^2} - R \approx \pm x - y + \frac{x^2 + y^2}{2R} \quad , \tag{1}$$

where x and y are displacements parallel and perpendicular to the interferometer baseline and R is a fixed distance (800 mm) from the x-y plane to the baseline corner cubes. The translations x and y vary within a circle of radius 100 mm. From Eq. (1) it is clear that the path length difference between the two IIPS arms (*i.e.*, the external delay) is precisely 2x giving a total one-way range of ±200 mm. Note that the external delay is independent of y; this is useful when we want to remove certain bias terms that are described in Sec. 1.3.

1.3 Field dependent bias terms

The SIM instrument operates in two basic modes, so called wide angle (WA) and narrow angle (NA). The WA mode covers a patch of sky (called a tile) 15 degrees in diameter while the NA mode coverage is 1 degree in diameter. Both modes involve macro changes[3] in the pointing of the science interferometer collecting optics (called siderostats) and adjustments to the optical path in one arm depending of the field point being observed. These macro configuration changes, resulting from a change in field angle, produce a class of systematic biases to the measurement of the external delay. Because these biases are explicit functions of field angle, they are termed field dependent (FD) biases. These biases can be classified in three categories: (1) diffraction, (2) beam walk, and (3) corner cube related phenomena. In this section we give a brief overview of the nature of these FD biases. In Sec. 2 we describe the models for each of these biases in detail.

The diffraction bias term results from two facts: (1) the internal metrology and starlight beams have different wavelengths, beam geometries, and propagation lengths, and (2) the pathlength in one arm of the interferometer must be

[3] Macro changes to the system configuration can be thought of as intentional, or commanded, changes. This is to be contrasted with micro system configuration changes that, in general, are smaller in magnitude and result from thermal distortions and dynamic disturbances.

varied to compensate for changes in the external delay as the field point changes. The change in the average phase of the metrology and starlight beams can be thought of as composed of a geometric part and a diffraction part. Since the metrology and starlight beams travel the same path[4] the geometric contribution to phase change is removed by the data processing leaving the difference of the diffraction terms. Although the metrology and starlight beams have different wavelengths, beam geometries, and propagation path lengths, the parameter of interest when comparing differences in the diffraction terms is the Fresnel number. The Fresnel number is a function of wavelength, beam geometry and propagation pathlength as indicated in Eq. (2) below.

$$N_F = \frac{w^2}{\lambda z} \quad , \tag{2}$$

where w is half the characteristic dimension of the diffracting aperture (*i.e.*, radius for a circle or half the side for a square), λ is the wavelength, and z is the propagation distance. Beams that differ in wavelength, geometry, and propagation length, but have the same Fresnel number, will have the same diffraction term.

The beam walk bias term refers to the path length change that results from the translation of a beam over the imperfect surface of an optical component such as a mirror. That is, there is a change in the average phase of the beam without any change in the position of the optic. The beam walk bias term is a function of the beam geometry, the rms surface figure error, the power spectral density (PSD) function of the surface profile, and the beam translation distance. In order to model beam walk in a deterministic manner one would need to know the surface profile of each optic with high spatial resolution and the terminal points of the beam translation relative to the surface profile. Rather than a deterministic calculation, our beam walk model relies on a statistical approach. Beam walk can result from both field independent (FI) and dependent processes. For example, misalignment of a mirror due to thermal gradients will produce FI beam walk on the downstream optics. On the other hand, axial translation of the delay line optic (a corner cube) on rails that are misaligned with respect to the beam propagation direction will produce a FD beam walk.

The baselines of the four SIM interferometers are defined by corner cubes as previously mentioned. The corner cubes are also the only components in the instrument that the internal and external metrology beams have in common. For the science baselines, the corner cubes are embedded in the siderostat mirrors and thus articulate as the interferometer observes different stars in a particular tile. As the corner cubes articulate the internal and external metrology beams are incident on the cube facets at changing angles and intercept points. As a result there are changes in the average phase of the metrology beams due to changes in reflection phase shifts and dihedral errors. The design of the corner cube surfaces calls for coating with unprotected gold. Thus, the reflection phase shift is a function of the polarization state of the incident field and varies continuously with angle of incidence. Dihedral errors refer to the fact that the corner cube facet normals are not exactly mutually perpendicular. This gives rise to geometric path length errors that depend on reflection sequence and point of incidence.

There are three additional FD corner cube errors to consider: (1) corner cube vertex/siderostat offset, (2) non-common vertices, and (3) beam walk. The first effect refers to the fact that the corner cube vertex is offset from the surface of the siderostat mirror. This introduces a non-common optical path between the starlight and the internal metrology that varies with field angle. The second item results from the need to accommodate both internal and external metrology beams whose propagation directions exceed the field of view of a single corner cube. We have effectively extended the field of view of the corner cubes by utilizing assemblies that are multiple corner cubes. In theory these multiple corner cubes have a common vertex but in practice they do not due to fabrication limitations. The non-common vertex bias does not appear in MAM because there is no external metrology system; however, this error is important for the flight system so we mention it here for completeness. Finally, there are two types of beam walk to consider. The corner cube articulation axes will not pass through the vertex. The resulting translation of the corner cube facets relative to the fixed metrology beams will produce beam walk of the type described above. Another type of beam walk also occurs because the metrology beam footprints on the facets change shape as the corner cubes articulate.

---

[4] The metrology propagates through the system in double pass but the change in its phase is multiplied by 0.5. This removes the geometric contribution when the difference between the metrology and starlight phase change is computed.

In this section we have provided an introduction to the nature of the FD biases encountered in the MAM testbed. In the next section we give the details concerning the modeling of these bias terms.

2. FIELD DEPENDENT MODELS

2.1 Diffraction

The computer code used to model diffraction terms for the SIM flight system and testbeds was developed at the Lockheed Martin Advanced Technology Center by R. Benson [Ref. 3]. In this section we briefly describe some of the physical principles and numerical techniques on which the code is based. The SIM diffraction code is a numerical implementation of the scalar, paraxial theory as described in Ref. 4. Diffraction calculations for SIM consist of a series of free-space propagations between various planes within the optical system. The Fresnel numbers for these propagations vary over a wide range of values implying that both near field and far field calculations are required.[5]

The diffraction calculation can be formulated in a number of ways. Consider an aperture Σ in the x-y plane. Let a field of wavelength λ be incident on the aperture. We wish to calculate the field for an arbitrary observation point p_0 = (x,y,z). Following Ref. 4, we may write the complex field at p_0 in two formulations[6]

$$E(p_0) = \frac{1}{i\lambda}\iint_{\Sigma} E(p_1)\frac{\exp(ikr_{01})}{z}d\Sigma \quad , \tag{3a}$$

$$E(p_0) = \iint A(f_x, f_y, 0)\exp\left(ikz\sqrt{1-(\lambda f_x)^2-(\lambda f_y)^2}\right)\exp\left[i2\pi\left(xf_x+yf_y\right)\right]df_x df_y \quad , \tag{3b}$$

where k is the wave number $2\pi/\lambda$, p_1 is in Σ, r_{01} is the distance from p_1 to p_0, $f_q = \alpha/\lambda$ is the spatial frequency associated with the direction cosine α along the q axis, and A is the Fourier transform of the field in the aperture Σ. The expressions given in Eq. (3a) and (3b) may be called the point source, or direct method, and the angular spectrum method respectively. Although the two expressions are mathematically equivalent, there are computational advantages to having the capability of evaluating either expression depending on circumstances. The expressions in Eq. (3) are simplified by evoking the assumption that the propagation distance is much greater than the maximum linear dimension of either the aperture Σ or the region of interest in the observation plane. Expanding the appropriate square roots yields

$$r_{01} \cong z + \frac{(x_1-x_0)^2}{2z} + \frac{(y_1-y_0)^2}{2z} \quad , \tag{4a}$$

$$\sqrt{1-(\lambda f_x)^2-(\lambda f_y)^2} \cong 1-\frac{1}{2}\left[(\lambda f_x)^2+(\lambda f_y)^2\right] \quad , \tag{4b}$$

Substituting Eqs. (4) into (3) gives the following

$$E(p_0) = \frac{e^{ikz}}{i\lambda z}\exp\left[\frac{ik}{2z}\left(x_0^2+y_0^2\right)\right]\iint E(p_1)\exp\left[\frac{ik}{2z}\left(x_1^2+y_1^2\right)\right]\exp\left[\frac{i2\pi}{2z}\left(x_0x_1+y_0y_1\right)\right]dx_1dy \quad , \tag{5a}$$

$$E(p_0) = e^{ikz}\iint A(f_x, f_y, 0)\exp\left[-i\pi\lambda z\left(f_x^2+f_y^2\right)\right]\exp\left[i2\pi\left(xf_x+yf_y\right)\right]df_x df_y \quad . \tag{5b}$$

Inspection of Eq. (5) shows that for a fixed grid size (*e.g.*, NΔx) there is an exponential function within the integral of the direct method with an argument that is proportional to the Fresnel number; for the angular spectrum method the

---

[5] Near and far field diffraction calculations are often referred to as Fresnel and Fraunhofer approximations of the diffraction problem respectively. Technically, the Fresnel approximation covers both the near and far field; that is, the Fraunhofer integral is a special case of the Fresnel integral.

[6] In Eq. (3) the obliquity factor has been approximated as unity in keeping with the paraxial assumption.

argument is inversely proportional to the Fresnel number. Therefore, the integrand for the direct method becomes more oscillatory with increasing Fresnel number while the integrand for the angular spectrum method becomes more oscillatory with decreasing Fresnel number. Following the aliasing argument presented by Dutta and Benson [Ref. 3], we can cast the choice between Eqs. (5a) and (5b) in terms of propagation length as follows

$$z \le \frac{(N\Delta x)^2}{\lambda N} \Rightarrow \text{angular spectrum method} \quad , \tag{6a}$$

$$z \ge \frac{(N\Delta x)^2}{\lambda N} \Rightarrow \text{direct method} \quad . \tag{6b}$$

This trade in computational accuracy, as a function of Fresnel number, between the direct and angular spectrum methods was tested for a series of cases with closed-form solutions and demonstrated the need for both algorithms if a wide range of Fresnel numbers is required [Ref. 5]. Thus, the diffraction code chooses the appropriate formulation based on the criteria given in Eq. (6).

Both the direct and angular spectrum methods require numerical implementation of a two-dimensional Fourier transform that is usually called a discrete Fourier transform (DFT). A subset of DFT algorithms, called fast Fourier transforms (FFT), have been developed for high computational efficiency. However, FFTs come with certain restrictions on sample spacing in the two planes of interest. That is, selecting the sampling interval in one plane determines the sampling interval in the other plane. The general DFT does not contain this sampling restriction. Thus, what one sacrifices in computational speed is offset by the ability to tailor the sample spacing to the aperture of interest. However, one can improve the computational efficiency of the DFT by using the chirp z-transform (CZT) [Refs. 6, 7]. The CZT algorithm allows one to formulate the DFT as a convolution that can then be evaluated by FFT thus improving the computational speed over the DFT while retaining the freedom to choose the grid spacing in the transform plane. For the angular spectrum method, the diffraction code evaluates the Fourier transforms by a FFT. For the direct method, the code will use a FFT or the CZT depending on the user's choice for the grid spacing in the final plane.

Perhaps the most crucial issue with regard to diffraction is the accuracy of the code. This is a two-part question, namely (1) what is the accuracy requirement for SIM, and (2) how does one test the code. The answer to the first part of the question comes from the SIM astrometric error budget that requires knowledge of certain types of diffraction effects at the few picometer level.[7] The second part of the question required a two-step answer. Step 1 consisted of a computational check using a case amenable to implementation by an independent calculation using symbolic software such as Mathematica. This step checked that the paraxial, scalar diffraction equations were correctly coded in the Fortran program and gave an indication of the accuracy as a function of sample spacing. To make the calculation tractable in Mathematica we chose a case with circular symmetry and calculated the average phase of the beam in the observation plane. The circular symmetry allowed us to replace two-dimensional DFTs with one-dimensional Fourier-Bessel transforms. The Mathematica calculation was carried out with a working precision of 34 digits[8] and was taken as the "correct" answer. The difference in average phase, converted to path length (λ = 1.319 μm), between the Fortran diffraction code and the Mathematica calculation, as a function of sample spacing, is given in Table 1. Based on the convergence of the two methods at the picometer level, as a function of sample spacing, we concluded that the Fortran diffraction code algorithms were properly coded and had the necessary precision.

Table 1: Comparison of Fortran and Mathematica diffraction calculations

Grid size (mm)	Grid pts.	Sample spacing (μm)	Average phase difference (pm)
50	2048	24.4	16
25	2048	12.2	4
25	4096	6.1	1

[7] The metrology beam launchers have a requirement on an error called cyclic error that is 3 pm.

[8] A working precision of 34 is the precision used for internal calculations. We used the default setting for the precision of the final answer (precision goal parameter) which means the calculation strives for 10 digits less or 24 digits of precision.

The Fortran code and the Mathematica calculations embody the same paraxial, scalar approximations. Thus, step 2 of the verification process was to check the code against a set of measurements. A special testbed, dubbed the Diffraction testbed (DTB), was designed and constructed at the Lockheed Martin Advanced Technology Center for this purpose [Ref. 8]. The details of the configuration, operation, and data processing of the DTB are outside the scope of this paper but suffice it to say that the testbed was designed to operate with SIM-like starlight and metrology Fresnel numbers. There were several requirements levied on the agreement between the diffraction model and the DTB results but the most germane for our discussion is the following: The rms difference between the DTB and model OPD residuals (obtained by removing linear and quadratic terms) shall be less than 75 pm over a 30-cm mechanical delay line stroke. The model and testbed rms difference was 43 pm and thus met this requirement with margin. This was a truly impressive achievement for both the testbed and the model. It should also be noted that the DTB is the first successful SIM pico-level testbed.

2.2 Beam walk

The beam walk model is a statistical calculation. The quantity calculated is the standard deviation of a zero-mean distribution of path length changes that result from translation of a beam of given geometry by a distance $\vec{s}$ over an ensemble of surfaces that are all characterized by a specified diameter, rms surface figure error, and PSD function for the surface error. The general expression for the variance of this path length change, σ^2, is given by the following expression.

$$\sigma^2 = \left\langle \left| \frac{1}{A}\int x(\vec{r})\,d\vec{r} - \frac{1}{A}\int x(\vec{r}+\vec{s})\,d\vec{r} \right|^2 \right\rangle \quad , \tag{7}$$

where x is the deviation of the surface height from the mean at position $\vec{r}$, A is the area of the beam, and <...> represents an average over an ensemble of surfaces. The beam walk calculation is based on a formalism used for random processes in atmospheric turbulence problems. The key concept is the representation of the optic surface in Eq. (7) by a stochastic Fourier Stieltjes integral as described in Appendix A of Ref. 9 and given in Eq. (8). The use of this integral representation for beam walk analysis was originally developed at JPL by M. Colavita.

$$x(\vec{r}) = \int_{-\infty}^{\infty} \exp\left(-i2\pi\vec{f}\cdot\vec{r}\right) d\omega\left(\vec{f}\right) \quad , \tag{8}$$

where f is the spatial frequency normalized to the mirror diameter and dω(f) is called the random amplitude. The random amplitude has the following property

$$\left\langle d\omega\left(\vec{f}\right) d\omega\left(\vec{f}'\right)\right\rangle = PSD\left(\vec{f}\right)\delta\left(\vec{f}-\vec{f}'\right)d\vec{f}\,d\vec{f}' \quad . \tag{9}$$

In order the carry out this calculation we make several assumptions that are listed here:

- The PSD function is radially symmetric; hence, the path length change only depends on the magnitude of the walk and not the direction.
- The PSD function is directly proportional to f^p. If PSD data are available we fit for the exponent p. If no data are available we usually assume p = -2.5. The minimum spatial frequency considered is 1 cycle/mirror diameter.
- One half of the surface error power is contained in spatial frequencies greater than 1 cycle/mirror diameter.

Using Eqs. (7) – (9) and the assumptions listed above, the general form for the path length change variance can be written as an integral of spatial frequencies over the PSD function, normalized to half the wavefront variance, multiplied by a transfer or filter function H.

$$\sigma^2 = 2\pi\int_1^{\infty} PSD(f)H(f)f\,df \quad . \tag{10}$$

As an example, the filter function for a uniform circular beam of diameter d, normalized to the mirror diameter, is

$$H(f) = 2\left[1 - J_0(2\pi f s)\right]\left[\frac{2J_1(\pi f d)}{\pi f d}\right]^2 \quad , \tag{11}$$

where J_0 and J_1 are Bessel functions of the first kind of order 0 and 1 respectively.

We are often interested in a quantity called the beam walk sensitivity that is the first derivative of the path length change standard deviation with respect to beam translation. For a circular beam and typical beam/mirror dimensions, it can be easily shown that σ is a linear function of s. Expanding J_0 as a power series of its argument yields [Ref. 10]

$$J_0(z) \cong 1 - \frac{z^2}{4} \qquad \text{for } z << 1 \quad . \tag{12}$$

Substituting Eqs. (11) and (12) into (10) shows that σ is directly proportional to s. Thus, for this case and many others, the beam walk sensitivity is independent of the magnitude of the beam translation.

A secondary goal of the DTB was to validate the beam walk model described above. Note that it is difficult to assign a pass/fail criterion to this test due to the statistical nature of the model. The beam walk sensitivity results for the testbed and the model were 0.53 and 0.90 pm/μm respectively. Analysis of various model uncertainties showed that the model prediction could reasonably be 0.74 pm/μm. It was concluded that the agreement between the testbed and the model was close enough that there is unlikely to be anything substantially incorrect about the model assumptions or computational techniques. A detail discussion of the beam walk test and model results can be found in Ref. 8.

2.3 Corner cubes

2.3.1 Dihedral errors

The dihedral error between two corner cube facets is the difference of the angle between the surface normals and 90 degrees. These errors result in two types of geometric path length changes as the corner cube articulates, namely OPD_1 within the corner cube and OPD_2 due to the fact that a given ray exiting the corner cube is no longer propagating anti-parallel to the incident ray direction. An expression for the first type of OPD between two facets is easily derived. Consider the path length of a ray propagating between facet i and j. The facets are defined by their unit normals, n_i and n_j, and the corner cube vertex q. Let the ray of interest be incident on facet i at the point p_i and propagate between surfaces i and j along the unit vector v. Then the propagation distance t between facets i and j is given by the following equation.

$$t = \frac{\langle q - p_i, n_j \rangle}{\langle v, n_j \rangle} \quad , \tag{13}$$

where <a , b> is the inner product between vectors a and b. Let ψ be the dihedral error between facets i and j. To first order in ψ we may write $n_j = r + \psi n_i$ where r is the unit normal to facet j with no dihedral error present. Substituting this expression for n_j into Eq. (13) yields after some manipulation the following

$$OPD_1 = t - \frac{\langle q - p_i, r \rangle}{\langle v, r \rangle} = -\psi \langle q - p_i, r \rangle \frac{\langle v, n_i \rangle}{\langle v, r \rangle^2} \quad . \tag{14}$$

We note that OPD_1 is directly proportional to the dihedral error and the distance between the ray intercept on facet i and the corner cube vertex. In addition, the proportionality constant is a function of the angle of incidence at facet i.

To calculate OPD_2 we need to know the propagation direction of a ray exiting the corner cube compared to the incident ray direction, that is, the angle of deviation θ. It can be shown [Ref. 11] that

$$\theta = 2|v \times \psi| \quad , \tag{15}$$

where v is a unit vector in the incident propagation direction and ψ is a vector containing the three dihedral errors defined as follows when the subscripts denote the reflection sequence.

$$\langle n_1, n_2 \rangle = \psi_3 \; ; \quad \langle n_1, n_3 \rangle = -\psi_2 \; ; \quad \langle n_2, n_3 \rangle = \psi_1 \quad . \tag{16}$$

Using the expression in Eq. (15) for the propagation deviation angle, the value of OPD_2 after propagating a distance L is given by

$$OPD_2 = 2L|v \times \psi|^2 \quad . \tag{17}$$

Comparing Eqs. (14) and (17), it is clear that the OPD within the corner cube depends on the dihedral error to first order while the OPD resulting from misalignment is a second order effect. The implication of the above analysis is that each ray will have its particular OPD based on its reflection sequence and point of incidence.

2.3.2 Reflection phase shifts

Reflection phase shifts are a function of angle of incidence, wavelength, index of refraction of the reflecting surface, and polarization state. In the case of MAM only the articulation of the corner cubes at the siderostats will produce significant changes in the reflection phase shifts. The corner cubes are coated with unprotected gold and hence have a complex index of refraction. The reflection phase shifts are given by the well-known Fresnel equations. The only issue involves consistency between the Fresnel equations, the directions of the s and p polarization unit vectors before and after the reflection, the sign of the imaginary part of the complex index, and the sign of the spatial phase term for a wave propagating in free space. We have found several inconsistencies between these items in various texts and commercial optical design codes. A complete discussion of these issues can be found in Ref. 12. We can summarize our modeling conventions as follows: (1) The spatial part of the phase of a wave propagating in free space becomes more positive in the direction of propagation. (2) The complex index of refraction is given by $\tilde{n} = n + ik$ where n and k are positive. (3) The positive (zero phase) directions of the incident and reflected p-polarization unit vector point are defined by the cross product s x k where s is the unit vector in the positive s-polarization direction and k is the propagation vector. (4) Finally, the equations for the s- and p-polarization complex amplitude reflection coefficients are given by

$$R_s = -\frac{\sin(\theta_i - \theta_r)}{\sin(\theta_i + \theta_r)} \quad and \quad R_p = \frac{\tan(\theta_i - \theta_r)}{\sin(\theta_i + \theta_r)} \quad , \tag{18}$$

where θ_i and θ_r and the angles of incidence and refraction respectively.

2.3.3 Vertex offset

The siderostat mirror articulates over the field of regard to reflect IIPS starlight, defined by the unit vector s, into the TA optical system in a direction specified by the unit vector e. If the corner cube vertex is separated from the siderostat front surface by a distance d along the mirror normal, the unmonitored geometric distance, b, is given by

$$b = d\sqrt{2 + 2\langle s, e \rangle} \quad , \tag{19}$$

where <s , e> is the inner product between the vectors s and e. The unmonitored distance at the center of the field of regard represents a constant offset between starlight and metrology path lengths that can be lumped in with other constant offsets. However, b is a function of field angle; thus, we are really interested in the deviation of b from its value

at the center of the field as a function of field angle. Although we can simply evaluate Eq. (19) for various field points, it is of interest to decompose this deviation into terms of increasing order of the field coordinates.

In the MAM testbed field angle is specified by the Cartesian coordinates x and y which are displacements from the center of the field in directions parallel and perpendicular to the TA baseline respectively. Let θ be the angle between the center of the field (x = y = 0) and the vector e. Then we can rewrite Eq. (19) as

$$b(x,y) = \sqrt{2}\, d\sqrt{1+\cos\theta}\,\frac{\sqrt{1+\langle s,e\rangle}}{\sqrt{1+\cos\theta}} = C\sqrt{1+K} \quad , \tag{20}$$

where C is the value of b and the center of the field and

$$K = \frac{y}{R}\frac{\sin\theta}{1+\cos\theta}\left(1-\frac{r^2}{2R^2}\right) - \frac{r^2}{2R^2}\frac{\cos\theta}{1+\cos\theta} \quad , \tag{21}$$

where $r^2 = x^2 + y^2$ and R is the distance between the corner cube vertex and the x-y plane. Expanding the radical in Eq. (20) as a power series in K, we may write the deviation of b from its value at the center of the field as a sum of terms of increasing order of the field coordinates noting that there is only a linear term in the field coordinate y.

$$linear\ \ term = \frac{C}{2}\frac{y}{R}\frac{\sin\theta}{1+\cos\theta} \quad , \tag{22a}$$

$$quadratic\ \ term = -\frac{C}{4R^2}\left\{r^2\frac{\cos\theta}{1+\cos\theta} + \frac{y^2}{2}\left(\frac{\sin\theta}{1+\cos\theta}\right)^2\right\} \quad , \tag{22b}$$

$$cubic\ \ term = \frac{C}{4R^3}\left\{\frac{y^3}{4}\left(\frac{\sin\theta}{1+\cos\theta}\right)^3 + \frac{yr^2}{2}\frac{\sin\theta\cos\theta}{(1+\cos\theta)^2} - yr^2\frac{\sin\theta}{1+\cos\theta}\right\} \quad . \tag{22c}$$

3. COMPARISON OF MODELS AND MAM DATA

In Section 2 we described the physical and mathematical bases of the various FD bias models. In some cases the model description applied to a single reflection or propagation path. These equations have been combined with a layout of the MAM testbed to produce system-level predictions. For computational reasons two system models have been developed, namely one for diffraction and one for corner cube phenomena. Beam walk calculations are not included in the results given below.

When comparing the model predictions with MAM data it is convenient to expand the FD bias function, α, in terms of the low-order Zernike polynomials written in Cartesian coordinates as in Eq. (23).

$$\alpha(x,y) = c_0 + c_1 x + c_2 y + c_3\left(x^2+y^2\right) + c_4\left(x^2-y^2\right) + c_5\, xy + \ldots, \tag{23}$$

where x and y are the MAM field coordinates parallel and perpendicular to the baseline respectively. Generally, we evaluate c_1, c_2, and c_3. Under certain circumstances we evaluate $c_3 + c_4$ and $c_3 - c_4$ which are the coefficients of x^2 and y^2 respectively. It is important to note that post-processing of the SIM flight system data will remove terms c_0 through c_3. For model validation purposes we compare coefficients c_1, c_2, $c_3 + c_4$, and $c_3 - c_4$ and the residual that remains after these terms are removed from the bias function α.

Validation of the diffraction model was successfully carried out on the DTB [Ref. 8]. However, in the interest of understanding the behavior of the MAM testbed we compare the model and testbed data for the diffraction bias term. Validation of the corner cube model is dependent on the comparison between model predictions and testbed data.

There are two criteria of interest over the WA field of regard, one pertaining to unprocessed data (only c_0 removed) and one to the residual after SIM-like post-processing. These criteria are written quantitatively as follows:

$$\max\left(\left|\alpha_{\mathrm{mod}}-\alpha_{MAM}\right|\right)/\left(\max\{\alpha_{MAM}\}-\min\{\alpha_{MAM}\}\right)<20\% \quad , \tag{24a}$$

$$rms\left(\tilde{\alpha}_{\mathrm{mod}}-\tilde{\alpha}_{MAM}\right)<61\ pm \quad , \tag{24b}$$

where α_{mod} and α_{MAM} represent the corner cube bias function for the model and testbed respectively. The superscript ~ indicates that the linear (c_1 and c_2) and quadratic terms ($c_3 + c_4$ and $c_3 - c_4$) have been removed.

In order to facilitate the comparison of the MAM models and experimental results the testbed was operated in particular modes that isolated, to varying degrees, the various bias terms.[9] To isolate the diffraction term the testbed was run in the TA and IIPS retro modes that utilize only half of the testbed at a time. For example, in the TA retro mode the siderostats are oriented to retro-reflect a monochromatic starlight source that propagates with the internal metrology beam from the TA beam splitter. In this case the TA operates entirely without the IIPS. Because the starlight source has a long coherence length the TA can still produce fringes for large path length differences. Thus, the only macro configuration change in this mode is the path length in the TA arm with the delay line. For the corresponding mode on the IIPS side the siderostats are replaced with large corner cubes that return the metrology and starlight beams. The corner cubes articulate to give them a constant orientation with respect to the starlight and metrology beams and thus remove their FD effects. To isolate the corner cube effects we operate the testbed in its normal IIPS plus TA configuration but only analyze data that depend on the coordinate perpendicular to the TA baseline. Motion in this direction maintains a constant path length difference thus producing a constant diffraction contribution. Another test of the corner cube model is the IIPS retro test where only the corner cubes articulate. In this case the path lengths in each arm are fixed so that the diffraction term is a constant. At this time the dihedral errors for the corner cubes used in the IIPS retro test have not been measured with sufficient precision. Thus, comparison between the model and IIPS test data will not be available until the tests have been completed, the large corner cubes removed and their dihedral errors re-measured.

3.1 Diffraction results

Table 2 compares the model results with the testbed data for the two tests that were intended to isolate the diffraction terms for the TA and IIPS. The TA retro mode test generates a true one-dimensional bias function in the field variable x because there is no other degree of freedom. Thus, only the coefficients c_1 and $c_3 + c_4$ are meaningful. On the other hand, the IIPS retro test produces a two-dimensional bias function although it is weakly dependent on the y coordinate. Both the model and testbed data show that the diffraction in the IIPS dominates the diffraction in the TA.

Table 2: Comparison of MAM data and model predictions for diffraction terms

	TA retro test		IIPS retro test	
Coefficient	Model	MAM data	Model	MAM data
c_1 (pm/deg)	388	-659	-1974	-2184
c_2 (pm/deg)	N/A	N/A	0.8	60
$c_3 + c_4$ (pm/deg^2)	12	81	-2.6	59
$c_3 - c_4$ (pm/deg^2)	N/A	N/A	-2.6	1.4

3.2 Corner cube results

The three corner cube phenomena described in some detail above have been integrated into a single model called the integrated model. However, it is possible to evaluate each term separately. For example, one can determine the reflection phase shifts assuming no dihedral errors or vertex offset. Thus, the sum of the individual terms can be compared with the fully integrated model. This exercise has been carried out with results that differ at the few picometer

[9] Note that all macro changes to the system configuration introduce beam walk which is not included in either the diffraction or corner cube models.

level. We therefore conclude that the coupling between reflection phase shifts, dihedral errors, and vertex offset is negligible for the size errors of interest to MAM and SIM. In addition to demonstrating that coupling between different corner cube bias terms is small, the individual models give insight into which type of corner cube errors dominate the overall bias function. For example we have found that the reflection phase shifts from the two arms largely cancel each other producing a small net bias term. Table 3 presents the c_2 and $c_3 - c_4$ coefficients derived from fits to the MAM measurements for the IIPS plus TA configuration along with the model predictions.

Table 3: Comparison of MAM data and model predictions for corner cube terms

	IIPS +TA	
Coefficient	Model	MAM data
c_1 (pm/deg)	N/A	N/A
c_2 (pm/deg)	1045	1218
$c_3 + c_4$ (pm/deg^2)	N/A	N/A
$c_3 - c_4$ (pm/deg^2)	-41	-26

A comparison of the unprocessed data between the model predictions and the testbed data gives a result of 11.3% against a goal of 20%. Comparing the model and testbed data residual functions yields an rms difference of 104 pm against a goal of 61 pm. This result represents two slices along the y-axis at x field angles of ±1 deg. A y-axis slice at x = 0 deg. was not used because there is only one test field point for this x coordinate (*i.e.*, x = y = 0). Larger x coordinates introduce unwanted diffraction terms and were not analyzed.

4. CONCLUSIONS

We have compared modeling results and testbed data for three cases. For the two cases with large linear terms, one for diffraction and one for the corner cubes, the agreement between model and data for these linear terms is approximately 10 and 15 percent respectively. For the diffraction case with the relatively small linear term (TA retro case), the sign and magnitude do not agree. For this case the sign and magnitude of the measured linear term is known to fluctuate with metrology and starlight beam alignment and perhaps other factors that are not known at this time. Thus, a reliable comparison will require, at the very least, an optimized and stabilized alignment between these starlight and metrology.

For the IIPS retro configuration the testbed reports a significant x quadratic coefficient that the model does not predict. Based on the model results and theoretical considerations, we believe that this coefficient should be very small. The origin of this quadratic term in the testbed results is currently under investigation.

Finally, the corner cube model has met the criterion given in Eq. (24a) with considerable margin. For the more stringent criterion given in Eq. (24b), the match up between the model and the test data exceeds the goal by 70%. A task for the immediate future is to determine if this discrepancy is consistent with our knowledge uncertainty of the pertinent testbed parameters. For the present, we believe the match between the model and test data is sufficiently close to indicate that all the significant physics has been correctly captured in the model.

ACKNOWLEDGEMENTS

The author would like to acknowledge the significant contributions of R. Goullioud (JPL), who has overall responsibility for the MAM testbed and provided valuable oversight of the modeling effort, and J. Shen (JPL), who performed all the MAM data analysis. This research was performed at the Jet Propulsion Laboratory, California Institute of Technology, under contract with the National Aeronautics and Space Administration.

REFERENCES

1. P. Kahn and K. Aaron, "Space Interferometry Mission: Flight system and configuration overview," Proc. of SPIE Vol. 4852, 2002, pp. 33-44.
2. B. Hines et al., "Micro-arcsecond metrology (MAM) testbed overview," Proc. of SPIE Vol. 4852, 2002, pp. 45-56.
3. K. Dutta and R. Benson, "Performance modeling of optical metrology systems," Proc. of SPIE Vol. 4852, 2002, pp. 839-848.

4. J. W. Goodman, *Introduction to Fourier Optics*, McGraw-Hill Book Company, San Francisco, 1968.
5. M. V. Papalexandris and D. C. Redding, "Calculation of diffraction effects on the average phase of an optical field," J. Opt. Soc. Am. A, 17, 2000, pp. 1763-1772.
6. L. R. Rabiner, R. W. Schafer, and C. M. Rader, "The Chirp z-Transform," IEEE Trans. Audio and Electroacoustics, AU-17, 1969, pp. 86-92.
7. S. Roose, B. Brichau, and E. W. Stijns, "An efficient interpolation algorithm for Fourier and diffractive optics," Optics Communications, 97, 1993, pp. 312-318.
8. D. S. Schaechter, Diffraction Testbed Final Report, JPL internal document D-21722, January 14, 2004.
9. A. Ishimaru, *Wave Propagation and Scattering in Random Media*, IEEE Press, Piscataway, New Jersey, 1997.
10. M. Abramowitz and I. Stegun, *Handbook of Mathematical Functions*, Dover Publications, Inc., New York, 1965.
11. M. Milman, private communication entitled "Corner cube stuff."
12. G. Kuan and R. Demers, "On Kite, Zemax, and Electric Field Propagation and Reflection," SIM library file 18704, March 17, 2004.

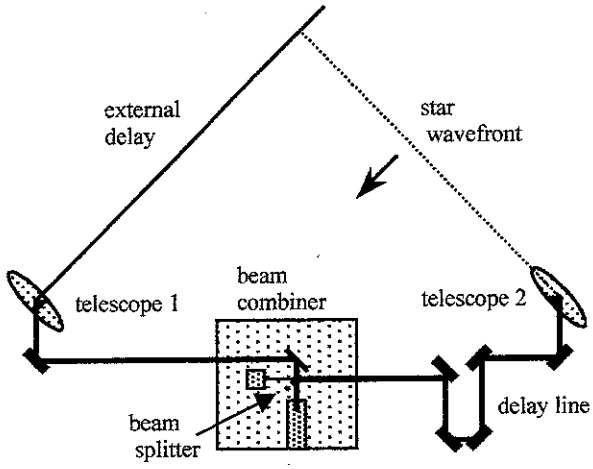

Fig. 1: Schematic of a SIM-like interferometer. The external delay is a function of the angle between the stellar wavefront and the interferometer baseline.

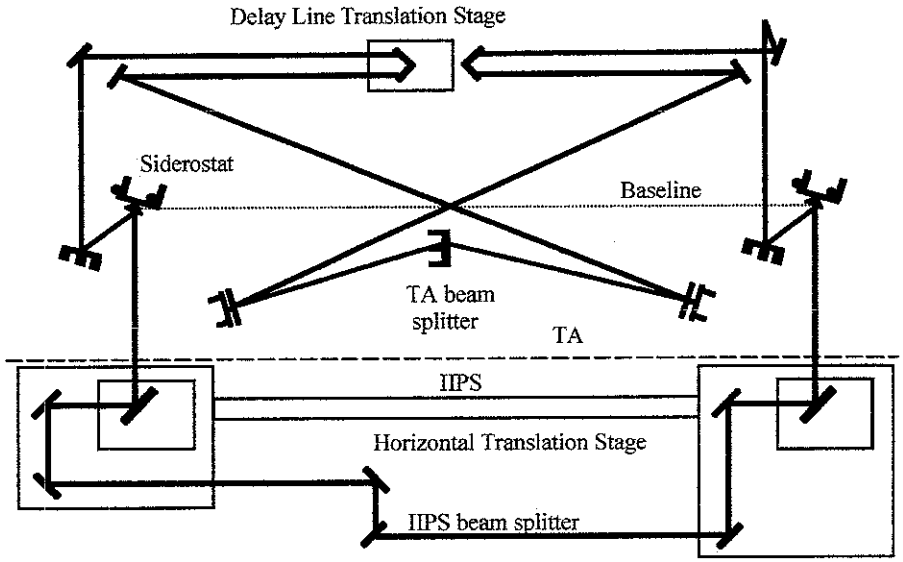

Fig. 2: Schematic of the MAM testbed. The dotted line indicates the boundary between the IIPS and the TA. The non-common paths extend from the IIPS beam splitter to the TA beam splitter.